

Impacts of Hurricane Irma (2017) on ocean transport processes

Thomas Dobbelaere^{a,*}, Milan Curcic^b, Matthieu le Hénaff^{c,d}, Emmanuel Hanert^{a,e}

^a*Eath and Life Institute (ELI), UCLouvain, Louvain-la-Neuve, Belgium*

^b*Rosenstiel School of Marine and Atmospheric Sciences (RSMAS), University of Miami, Coral Gables, Florida, USA*

^c*Cooperative Institute for Marine and Atmospheric Studies (CIMAS), University of Miami, Miami, Florida, USA*

^d*Atlantic Oceanographic and Meteorological Laboratory (AOML), NOAA, Miami, Florida, USA*

^e*Institute of Mechanics, Materials and Civil Engineering (IMMC), UCLouvain, Louvain-la-Neuve, Belgium*

Abstract

Tropical cyclones are becoming more intense and more frequent. Their effect is particularly acute in coastal areas where they cause extensive damage leading to an influx of debris, sediments and waste to the sea. However, most coastal ocean models do not represent heavy-wind transport processes correctly as they do not couple the hydrodynamics with the wind-generated waves. This may lead to significant errors during a tropical cyclone. Here, we investigate current-wave interactions during a major hurricane and assess their impact on transport processes. We do that by coupling the unstructured-mesh coastal ocean model SLIM with the spectral wave model SWAN, and applying it to the Florida Reef Tract during Hurricane Irma (Sept. 17). We show that the coupled model successfully reproduces the wave behavior, the storm surge and the ocean currents during the passage of the hurricane. We then use the coupled and uncoupled wave-current model to simulate the transport of

*Corresponding author

Email address: thomas.dobbelaere@uclouvain.be (Thomas Dobbelaere)

passive drifters. We show that the wave radiation stress gradient alone can lead to changes of up to 1 m/s in the modeled currents, which in turn leads to differences of up to 5 km in the position of drifting material over the duration of the hurricane. [Add a sentence on Stokes drift vs wave-current coupling]. Our results suggest that wave-current interactions can strongly impact the transport of drifting material such as sediments and debris in the aftermath of a hurricane. They should thus be taken into account in order to correctly assess its overall impact

Keywords:

1. Introduction

Tropical cyclones are becoming more intense and more frequent (Bhatia et al., 2019; Kossin et al., 2020). This increase is likely due to climate change and will probably continue in the future (Knutson et al., 2020). However, estimating the impact of tropical cyclones on the coastal ocean circulation remains a challenge. Understanding wave-current interactions and being able to represent their impact on coastal ocean transport processes is central to many coastal activities such as dredging, erosion management, O&G, search and rescue (Bever and MacWilliams, 2013; Li and Johns, 1998; Breivik et al., 2013). It would for instance allow to predict hurricane impacts in events such as the Deepwater Horizon oil spill in the Gulf of Mexico in 2010 (Le Hénaff et al., 2012).

Wave-current interactions during a cyclone are highly nonlinear and can vary significantly in space and time (Wu et al., 2011). Wave-induced currents are generated by wave radiation stress gradients (Longuet-Higgins, 1970), affecting water levels near shorelines and wave breaking points (Longuet-Higgins and Stewart, 1964). Changes in water levels and currents, in turn, affect the motion and evolution of the waves (Sikirić et al., 2013). Coupled wave-current models are therefore required to capture these complex interactions. In order to accurately include surface waves in their equations, such models require the

21 computation of the the full two-dimensional wave spectrum (Van Den Bremer
22 and Breivik, 2018). Spectral wave model are therefore needed.

23 Coastal oceans are characterized by the complex topography of the coast-
24 line and the presence of islands, reefs and artificial structures. Traditional
25 structured-grid models often lack the flexibility to simulate near-shore pro-
26 cesses at a sufficiently small scale. Instead, unstructured-mesh models can
27 easily adapt to the topography and are hence better suited to coastal processes
28 (Fringer et al., 2006; Chen et al., 2007). Being able to capture the impact
29 of the topography on wave interactions becomes even more important in
30 the case of tropical cyclones. Heavy winds generate large wind-waves and
31 disturb ocean conditions (Liu et al., 2020) by causing coastal upwellings on
32 continental shelves (Smith, 1982) and inducing strong currents, waves and
33 storm surges in nearshore and coastal regions (Dietrich et al., 2010; Weisberg
34 and Zheng, 2006).

35 The transport of drifting objects or substances that are locally released
36 is often best represented by a Lagrangian individual-based model. Such
37 an approach is routinely used to model the dispersal of larvae, pollutants,
38 sediments and many other tracers (e.g. Le Hénaff et al., 2012; Liubartseva
39 et al., 2018; Figueiredo et al., 2013; Frys et al., 2020). Although some transport
40 models take the impact of waves into account by adding a Stokes drift velocity,
41 *i.e.* the net drift of a floating particle in the direction of the wave propagation
42 (Van Den Bremer and Breivik, 2018), to the Eulerian currents, they usually
43 neglect the wave-induced currents. Such practice is reasonable in the case
44 of fair weather, when wave-induced forces exerted on currents are relatively
45 small, but might lead to significant errors during storm conditions (Röhrs
46 et al., 2012; Curcic et al., 2016).

47 The objective of this study is therefore to assess the importance of wave-
48 current interactions during a tropical cyclone. We investigate the transport
49 of drifting particles on the Florida shelf during Hurricane Irma, one of the
50 strongest and costliest tropical cyclones on record in the Atlantic Basin

51 (Xian et al., 2018), which made landfall in Florida in September 2017. To
52 do that, we developed an unstructured-mesh coupled wave-current model
53 of South Florida to simulate the ocean circulation during hurricane Irma.
54 Both modeled currents and waves were validated against field measurements
55 and then used to simulate the transport of drifting material in the Florida
56 Keys and the Florida inner shelf. Model outputs were then compared with
57 uncoupled simulation results in order to assess the impact of wave-induced
58 forces and Stokes drift on the modeled currents and transports.

59 **2. Methods**

60 *2.1. Study area and observational data*

61 The large-scale ocean circulation around South Florida is dominated by
62 the Florida Current (FC), which originates from the Loop Current (LC) where
63 it enters the Florida Straits from the Gulf of Mexico, and, downstream, forms
64 the Gulf Stream. The FC is a major western boundary current characterized
65 by spatial variability and meandering, associated with the presence of cyclonic
66 eddies between the core of the current and the complex reef topography
67 of the Florida Reef Tract (FRT) (Lee et al., 1995; Kourafalou and Kang,
68 2012). The variability of the FC extends over a large range of spatial and
69 temporal scales, with periods of 30-70 days in the Lower Keys (Lee et al., 1995)
70 and shorter periods of 2-21 days in the Upper Keys (Lee and Mayer, 1977),
71 and exhibits significant seasonal and interannual cycles (Johns and Schott,
72 1987; Lee and Williams, 1988; Schott et al., 1988). Circulation on the West
73 Florida Shelf (WFS), on the other hand, is forced by local winds and tidal
74 fluctuations (Lee and Smith, 2002; Liu and Weisberg, 2012). Furthermore,
75 due to its location relative to the warm waters of the North Atlantic, Florida
76 is particularly vulnerable to tropical cyclones. On average, the state gets
77 hit by a hurricane every two years and strong hurricanes, some of which are
78 among the most destructive on record, strike Florida on average once every
79 four years (Malmstadt et al., 2009).

80 The state of the ocean around Florida is monitored by an extensive
81 array of tide gauges, current meters and buoys. In this study, we used sea
82 surface elevation measurements from the National Oceanic and Atmospheric
83 Administrations (NOAA) Tides and Currents dataset. These measurements
84 were taken at four locations: two in the Florida Keys (Key West and Vaca Key);
85 one on the eastern coast of Florida (Virginia Key); and one on the western
86 coast (Naples). For the currents, we used ADCP measurements from the
87 University of South Florida's College of Marine Science's (USF/CMS) Coastal
88 Ocean Monitoring and Prediction System (COMPS) for the WFS (Weisberg
89 et al., 2009). More specifically, we used measurements from moorings C10,
90 C12 and C13, respectively located at the 25, 50, and 50 m isobaths of the
91 WFS (Liu et al., 2020). Finally, for the waves, we used measurements from
92 four buoys of the NOAA's National Data Buoy Center (NDBC); two on
93 Florida's eastern shelf and two on the WFS. The locations of all measurement
94 stations are shown in Fig. 1A,C.

95 *2.2. Wind and atmospheric pressure during Hurricane Irma*

96 Hurricane Irma made landfall in Florida on 10 September 2017 as a
97 category 3 hurricane, first at Cudjoe Key (Florida Keys) and later on Marco
98 Island, south to Naples (see hurricane track in Fig. 1). It then weakened to a
99 category 2 hurricane as it moved further inland (Pinelli et al., 2018). The
100 storm damaged up to 75% of the buildings at its landfall point in the Florida
101 Keys, making it one of the strongest and costliest hurricanes on record in the
102 Atlantic basin (Xian et al., 2018; Zhang et al., 2019). The strongest reported
103 wind speed was 50 m/s on Marco Island while the highest recorded storm
104 surge was 2.3 m, although larger wind speed likely occurred in the Florida
105 Keys (Pinelli et al., 2018). In order to reproduce the wind profile of Irma in
106 our model, we used high-resolution H*Wind wind fields (Powell et al., 1998).
107 As these data represent 1-min averaged wind speeds, we multiplied them by a
108 factor 0.93 to obtain 10-min averaged wind speeds (Harper et al., 2010), which
109 are more consistent with the time step of our model. Furthermore, H*Wind

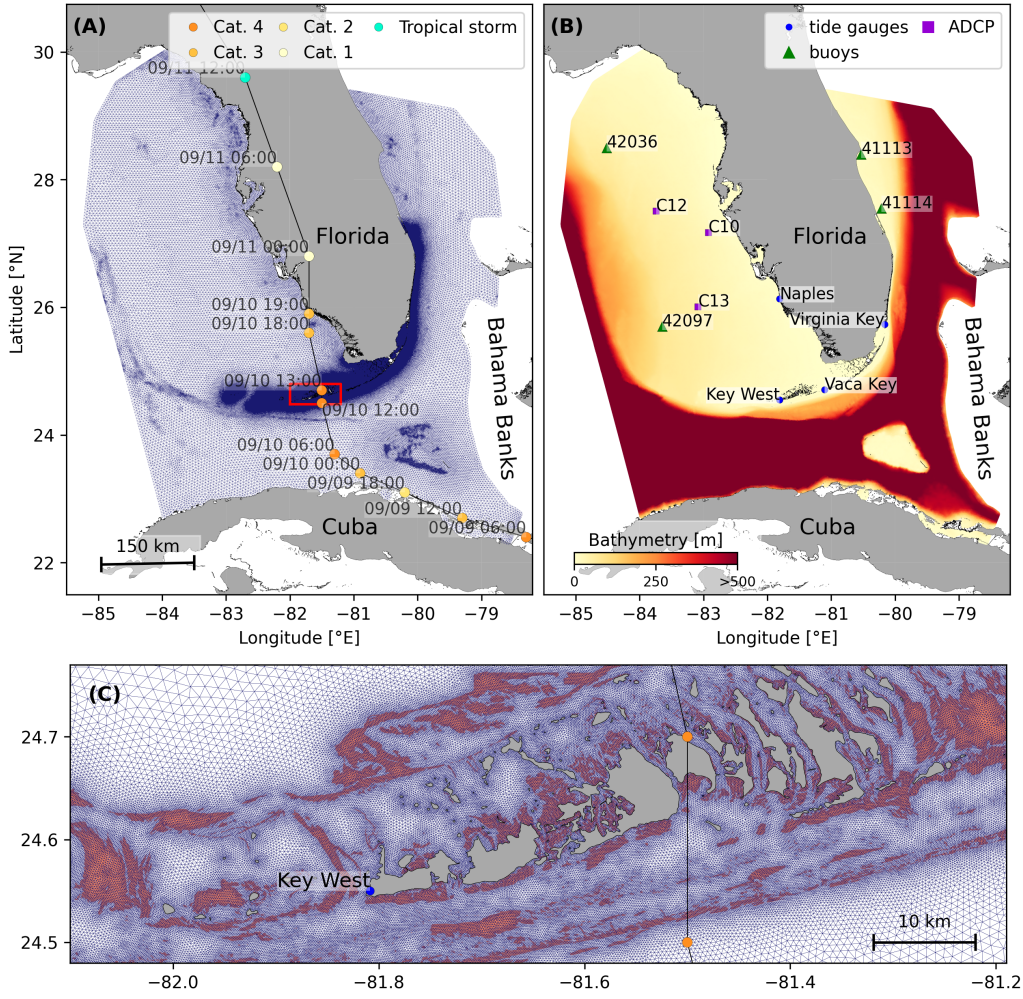


Fig. 1: (A) Mesh of the computational domain with the trajectory of Irma, the category of the hurricane is given by the Saffir-Simpson color scale. (B) Bathymetry of the domain with the location of stations used for the validation of the model outputs. (C) Close up view of the Lower Keys area, where the mesh resolution reaches 100m near reefs (shown in dark orange) and islands (highlighted in dark grey)

wind profiles did not cover the whole model extent during the passage of the hurricane and were thus blended within coarser wind field extracted from ECMWF ERA-5 datasets (Fig. 2A). The pressure field during the passage of Hurricane Irma was also reconstructed using ERA-5 data. However, the coarse resolution of the dataset smoothes out the depression at the center of the hurricane, leading to an underestimation of the pressure gradient (Fig. 2B). To better capture the central depression of Irma, we therefore built a hybrid pressure field using the position and the minimal pressure of the core of the hurricane based on its track as recorded in the HURDAT 2 database (Landsea and Franklin, 2013). Based on this information, the hybrid pressure field was constructed by combining an idealized Holland pressure profile (Lin and Chavas, 2012) within the radius of maximum wind speed of Irma (Knaff et al., 2018) with ERA-5 pressure field. The transition from the Holland profile to ERA-5 data outside the radius of maximum wind speed data was performed using a smooth step function (Fig. 2).

2.3. Hydrodynamic model

Ocean currents generated during hurricane Irma around South Florida were modeled using the 2D barotropic version of the unstructured-mesh coastal ocean model SLIM¹ (Lambrechts et al., 2008). The model mesh covers an area similar to the model extent of Dobbelaere et al. (2020), that includes the FRT but also the Florida Straits and part of the Gulf of Mexico (Figure 1). However, this area has been slightly extended northeastward and westward in order to include the NOAA-NDBC buoys. Furthermore, to withstand potential cell drying during the hurricane, we solved the conservative shallow

¹<https://www.slim-ocean.be>

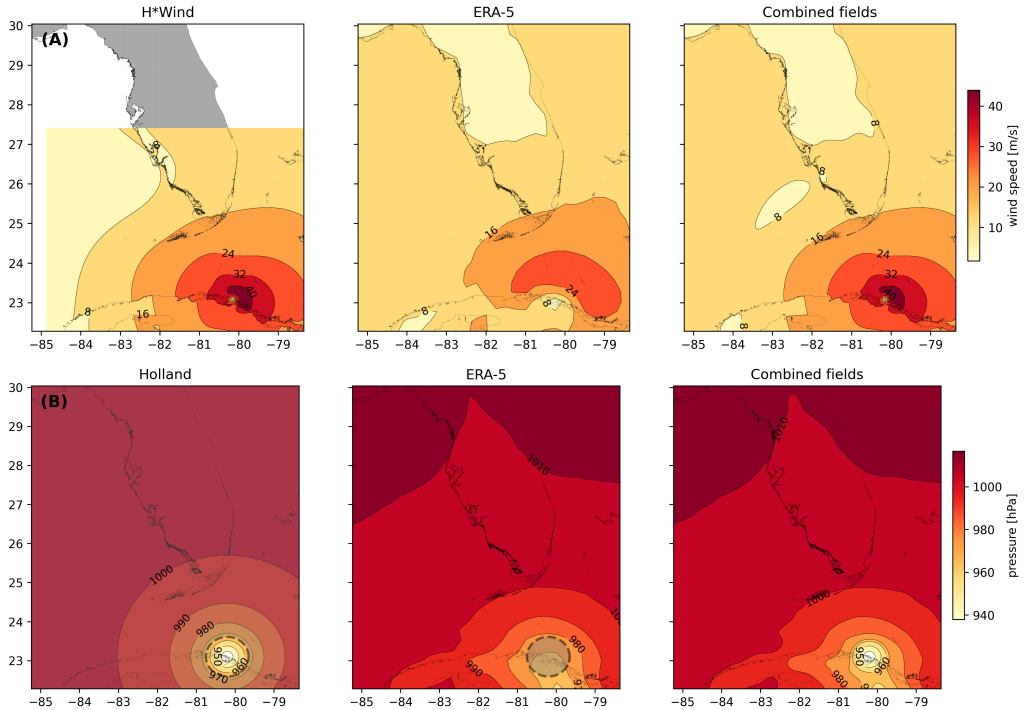


Fig. 2: Snapshot of the hybrid wind (A) and pressure (B) profiles constructed to capture the passage of Hurricane Irma at 1800 UTC on 9 September 2017. Wind profiles are obtained by combining high resolution H*Wind with coarser ERA-5 wind fields. The pressure field is built by combining the ERA-5 pressure field with an idealized Holland pressure profile based on the track of Irma in the HURDAT 2 database. Holland field was only used within the radius of maximum wind speed (dashed grey line) of the hurricane to capture its central depression.

₁₃₄ water equations with wetting-drying:

$$\begin{aligned} \frac{\partial H}{\partial t} + \nabla \cdot (\mathbf{U}) &= 0, \\ \frac{\partial \mathbf{U}}{\partial t} + \nabla \cdot \left(\frac{\mathbf{U}\mathbf{U}}{H} \right) + f\mathbf{e}_z \times \mathbf{U} &= \alpha g H \nabla(H - h) - \frac{1}{\rho} \nabla p_{\text{atm}} + \frac{1}{\rho} \boldsymbol{\tau}_s \\ &\quad + \nabla \cdot (\nu \nabla \mathbf{U}) - \frac{C_b}{H^2} |\mathbf{U}| \mathbf{U} + \gamma (\mathbf{U}_{\text{ref}} - \mathbf{U}), \end{aligned} \quad (1)$$

₁₃₅ where H is the water column height and \mathbf{U} is the depth-averaged transport;
₁₃₆ f is the Coriolis coefficient; g is the gravitational acceleration; h is the
₁₃₇ bathymetry; α is a coefficient indicating whether the mesh element is wet
₁₃₈ ($\alpha = 1$) or dry ($\alpha = 0$) (Le et al., 2020); ν is the viscosity; C_b is the
₁₃₉ bulk bottom drag coefficient; p_{atm} is the atmospheric pressure; $\boldsymbol{\tau}_s$ is the
₁₄₀ surface stress, usually due to wind; and γ is a relaxation coefficient towards a
₁₄₁ reference transport \mathbf{U}_{ref} . As in Frys et al. (2020) and Dobbelaere et al. (2020),
₁₄₂ SLIM currents were gradually relaxed towards the operational Navy HYCOM
₁₄₃ product (GOMl0.04², Chassignet et al. (2007)) in regions where the water
₁₄₄ depth exceeds 50m.

₁₄₅ At very high wind speeds, the white cap is blown off the crest of the
₁₄₆ waves. This phenomenon, also known as spumes, has been hypothesized to
₁₄₇ generate a layer of droplets that acts as a slip layer for the winds at the
₁₄₈ ocean-atmosphere interface (Holthuijsen et al., 2012). It causes a saturation
₁₄₉ of the wind drag coefficient for strong winds (Powell et al., 2003; Donelan
₁₅₀ et al., 2004; Curcic and Haus, 2020). We take this saturation effect into
₁₅₁ account by using the wind drag parameterization of Moon et al. (2007). In
₁₅₂ this parameterization, the drag coefficient C_d depends on the wind speed at

²<https://www.hycom.org/data/goml0pt04>

₁₅₃ 10-m height U_{10} according to:

$$C_d = \kappa^2 \log \left(\frac{10}{z_0} \right)^{-2} \quad (2)$$

₁₅₄ where κ is the von Karman constant and z_0 is the roughness length expressed
₁₅₅ as:

$$z_0 = \begin{cases} \frac{0.0185}{g} U_*^2 & \text{if } U_{10} \leq 12.5 \text{ m/s ,} \\ [0.085(-0.56U_*^2 + 20.255U_*) + 2.458] - 0.58] \times 10^{-3} & \text{if } U_{10} > 12.5 \text{ m/s ,} \end{cases} \quad (3)$$

₁₅₆ with U_* the friction velocity. The relation between U_{10} and U_* is given by:

$$U_{10} = -0.56U_*^2 + 20.255U_* + 2.458 . \quad (4)$$

₁₅₇ The mesh resolution depends on the distance to the coastlines and reefs
₁₅₈ following the approach of Dobbelaere et al. (2020). The mesh is then further
₁₅₉ refined according to bathymetry value and gradient, as suggested in the
₁₆₀ SWAN user-guide³. Such an approach improves the model efficiency as the
₁₆₁ mesh resolution is only increased where required by the currents and waves
₁₆₂ dynamics. The mesh was generated with the seamsh⁴ Python library, which is
₁₆₃ based on the open-source mesh generator GMSH (Geuzaine and Remacle,
₁₆₄ 2009). It is composed of approximately 7.7×10^5 elements. The coarsest
₁₆₅ elements, far away from the FRT, has a characteristic length of about 5 km
₁₆₆ whereas the finest elements have a characteristic length of about 100 m along
₁₆₇ the coastlines and over the reefs (Fig 1).

₁₆₈ *2.4. Wave model*

₁₆₉ Waves were modeled using the parallel unstructured-mesh version of the
₁₇₀ Simulating WAves Nearshore (SWAN) model (Booij et al., 1999), one of the

³<http://swanmodel.sourceforge.net/unswan/unswan.htm>

⁴<https://pypi.org/project/seamsh/>

171 most popular wave models for coastal areas and inland waters. It solves the
172 action balance equation (Mei, 1989):

$$\frac{\partial N}{\partial t} + \nabla_{\mathbf{x}} \cdot [(\mathbf{c}_g + \mathbf{u})N] + \frac{\partial}{\partial \theta}[c_\theta N] + \frac{\partial}{\partial \sigma}[c_\sigma N] = \frac{S_{in} + S_{ds} + S_{nl}}{\sigma}, \quad (5)$$

173 where $N = E/\sigma$ is the wave action density and E is the wave energy spectrum;
174 θ is the wave propagation direction; σ is the intrinsic wave frequency; \mathbf{c}_g is the
175 wave group velocity, $\mathbf{u} = \mathbf{U}/H$ is SLIM depth-averaged current velocity; c_θ
176 and c_σ are the propagation velocities in spectral space due to refraction and
177 shifting in frequency due to variations in depth and currents; and S_{in} , S_{ds} ,
178 and S_{nl} respectively represent wave growth by wind, wave decay and nonlinear
179 transfers of wave energy through interactions between triplets and quadruplets.
180 The wave spectra were discretized with 48 direction bins and 50 frequency
181 bins logarithmically distributed from 0.03 to 2 Hz. Exponential wind growth
182 was parameterized using the formulation of Janssen (1991), while dissipations
183 by whitecapping and bottom dissipations followed the formulations of Komen
184 et al. (1984) and Madsen et al. (1989), respectively.

185 Coefficients for exponential wind growth and whitecapping parameteriza-
186 tions were based on the results of Siadatmousavi et al. (2011), and significantly
187 differ from SWAN's default settings. By default, SWAN implements the wind
188 input formulation of Komen et al. (1984) and the steepness-dependent coeffi-
189 cient governing dissipation by whitecapping is a linear function of the wave
190 number. In this study, this steepness-dependent coefficient is a quadratic
191 function of the wave number, as it showed better predictions of the significant
192 wave height in the study of Siadatmousavi et al. (2011). The choice of these
193 formulations was motivated by the appearance of numerical instabilities in
194 the region of the Gulf Stream when using SWAN's default parameter values.
195 Finally, wave boundary conditions were derived from WAVEWATCH III
196 (Tolman et al., 2009) spectral outputs at NDBC buoy locations. We selected
197 these datasets as the large number of NDBC buoys around our region of
198 interest allowed for a fine representation of the wave spectra on the boundary

199 of the domain.

200 Surface waves induce a net drift in the direction of the wave propagation,
201 known as the Stokes drift (Van Den Bremer and Breivik, 2018; Stokes,
202 1880). This net drift has a significant impact on sediment transport in
203 nearshore regions (Hoefel and Elgar, 2003), on the formation of Langmuir
204 cells (Langmuir, 1938; Craik and Leibovich, 1976) as well as on the transport
205 of heat, salt or pollutants such as oil or micro-plastic in the upper ocean layer
206 (McWilliams and Sullivan, 2000; Röhrs et al., 2012; Drivdal et al., 2014). To
207 correctly model the Stokes drift profile in mixed wind-driven sea and swell
208 conditions, the full two-dimensional wave spectrum must be represented by a
209 spectral wave model within a wave-current coupling (Van Den Bremer and
210 Breivik, 2018). We therefore used SWAN modeled spectra to compute the
211 Stokes drift as follows:

$$\mathbf{u}_s = \int_0^{2\pi} \int_0^{+\infty} \frac{\sigma^3}{h \tanh(2kh)} E(\sigma, \theta) (\cos \theta, \sin \theta) d\sigma d\theta , \quad (6)$$

212 where k is the norm of the wave vector; h is the water depth; and $E(\sigma, \theta)$ is
213 the wave energy density.

214 2.5. Coupled model

215 SLIM and SWAN are coupled so that they run on the same computational
216 core and the same unstructured mesh. SLIM is run first and passes the
217 wind velocity (\mathbf{U}_{10}), water level ($\eta = H - h$) and depth-averaged current
218 ($\mathbf{u} = \mathbf{U}/H$) fields to SWAN, as well as a roughness length (z_0) for the bottom
219 dissipation formulation of Madsen et al. (1989). This roughness length is
220 computed from SLIM's bulk drag coefficient C_b following the approach of
221 Dietrich et al. (2011) so that both models have consistent bottom dissipation
222 parameterizations. SWAN then uses these quantities to compute the wave
223 radiation stress gradient, that is then passed to SLIM as the force exerted
224 by waves on currents $\boldsymbol{\tau}_{\text{wave}}$ (Fig. 3). SLIM then uses this quantity to
225 update the value of the surface stress $\boldsymbol{\tau}_s$ in Eq. (1), that now becomes

226 the sum of wind and wave-induced stresses $\tau_s = \tau_{\text{wind}} + \tau_{\text{wave}}$. Here, the
227 momentum flux from the atmosphere to the ocean is taken as the commonly-
228 used full wind stress τ_{wind} . Doing so, we neglect the momentum advected
229 away from the storm by the waves, leading to a 10-15% overestimation of the
230 momentum flux in hurricane winds (Curcic, 2015). Moreover, we followed
231 the approach of Dietrich et al. (2012) by characterizing the wave-induced
232 stresses using the radiation-stress representation instead of the vortex-force
233 representation (McWilliams et al., 2004). Although the later provides a clearer
234 and more meaningful decomposition of the wave effect, we implemented the
235 first representation for the sake of simplicity as it allows us to provide the
236 whole wave contribution as an additional surface stress to SLIM (Lane et al.,
237 2007).

238 SLIM's governing equations are integrated using an implicit time inte-
239 gration scheme while SWAN is unconditionally stable (Dietrich et al., 2012),
240 allowing both models to be run with relatively large time steps. In this study,
241 the stationary version of SWAN was used, *i.e.* the time derivative of Eq. (5)
242 was set to zero. This resulted in reduced scaling and convergence rates than
243 with the nonstationary version of SWAN but increased the stability of the
244 model. The wave spectra at each node of the mesh was saved at the end of
245 each iteration to serve as initial conditions for the next one. Both models
246 were run sequentially using a time step of 600 s, so that each computational
247 core was alternatively running either SLIM or SWAN. As in the coupling
248 between SWAN and ADCIRC (Dietrich et al., 2012), both models use the
249 same local sub-mesh, allowing for a one-to-one correspondence between the
250 geographic locations of the mesh vertices. No interpolation is therefore needed
251 when passing the discretised variables from one model to the other, which
252 allows an efficient inter-model communication. However, as SLIM is based on
253 a discontinuous Galerkin finite element method, an additional conversion step
254 to a continuous framework was required to transfer SLIM nodal quantities to
255 SWAN.

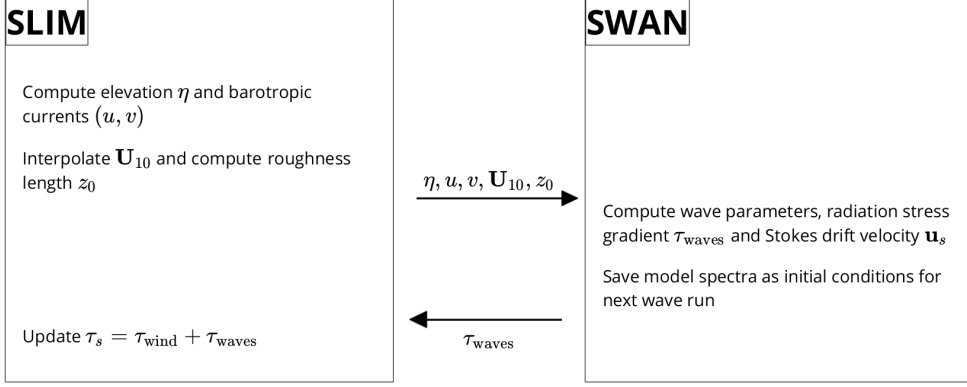


Fig. 3: Schematic illustration of the coupled SLIM+SWAN model.

256 *2.6. Quantifying the effect of wave-current interactions on transport*

257 To quantify the impact of wave-current interactions on transport processes,
 258 we compared the trajectories of passive particles advected by the uncoupled
 259 SLIM and coupled SLIM+SWAN currents during the passage of Irma in the
 260 Lower Keys. Furthermore, the depth-averaged Stokes drift was computed
 261 using the wave spectra of the coupled model SLIM+SWAN run as well as
 262 those of an uncoupled SWAN run. Particles were released on the inner and
 263 outer shelves at the points highlighted by red and blue dots in Fig. 4 on
 264 Sept. 7 at 0000 UTC and then tracked until Sept. 15. These initial particle
 265 positions were found using backtracking methods (Spivakovskaya et al., 2005)
 266 to ensure that the release particles would intersect the path of Irma during
 267 its passage through the Florida Keys. We first defined two 25 km² circular
 268 regions on the trajectory of the hurricane (see red and blue circles in Fig. 4).
 269 Particles within these two regions were then tracked backward in time using
 270 uncoupled SLIM currents from the exact time of the passage of the hurricane
 271 until Sept. 7 at 0000 UTC. Their positions at the end of the backward
 272 simulation (see red and blue particle clouds in Fig. 4) corresponds to the
 273 initial condition of the forward transport simulations described below. We
 274 then compared the trajectories of particles originating from these regions and

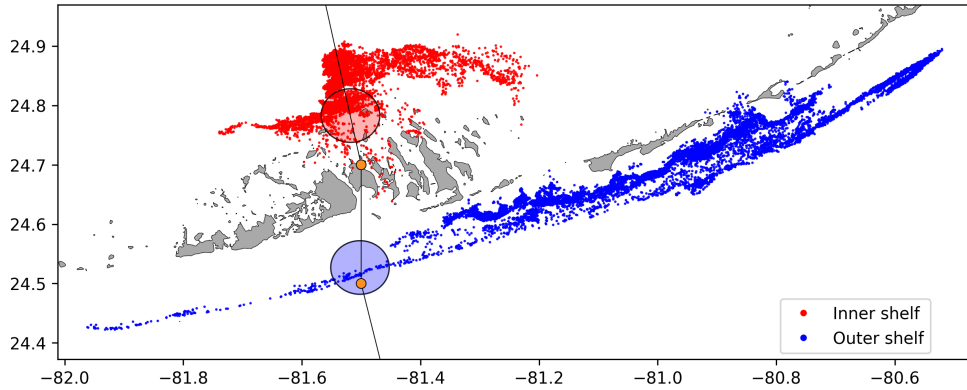


Fig. 4: Release regions of the passive particles on the inner and outer shelves (red and blue clouds) obtained by backtracking particles released in the red and blue circular areas during the passage of Irma.

advedted forward in time by different sets of currents: (i) uncoupled SLIM currents alone; (ii) coupled SLIM+SWAN currents; (iii) SLIM currents with the addition of the depth-averaged Stokes drift computed with the coupled wave-current model (Stokes-C); (iv) SLIM+SWAN currents with Stokes-C; and (v) SLIM currents with the depth-averaged Stokes drift computed with the uncoupled wave model (Stokes-U). Particles trajectories are compared by computing the distances between the centers of mass of the particle clouds through time.

3. Results

We first validated the reconstructed atmospheric fields of hurricane Irma as well as the outputs of our coupled wave-current model against field measurements. We then used the validated model outputs to simulate the transport of passive drifters in the Lower Keys during the passage of Hurricane Irma. These drifters were advected by the sets of currents described in section 2.6 and their trajectories were compared to evaluate the impact of the wave-current interactions and the Stokes drift on the transport processes during the passage of Irma.

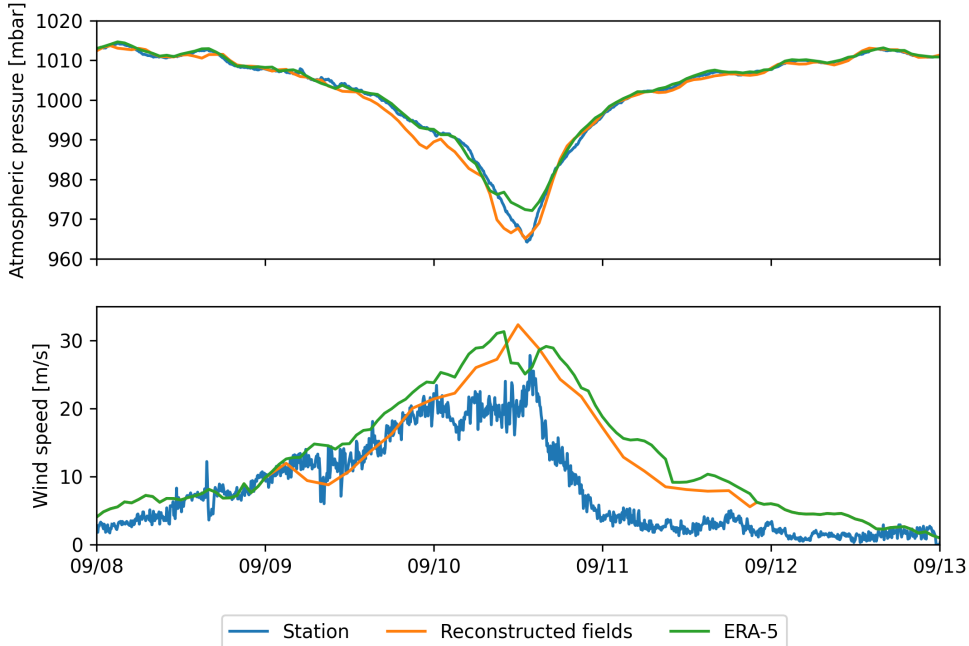


Fig. 5: Comparison of reconstructed wind atmospheric pressure with field measurements and coarser ECMWF ERA-5 profiles at Vaca Key station. The generated hybrid atmospheric forcings better reproduce the observed storm depression while H*wind winds better reproduce the measured peak in wind speed.

292 3.1. *Model validation*

293 H*Wind winds and hybrid pressure field agree well with station mea-
 294 surements at Vaca Key station (Fig. 5). The hybrid pressure field shows a
 295 better agreement with observations than ERA-5 pressure as it successfully
 296 reproduces the storm depression. ERA-5 fields, on the other hand, fail to
 297 reproduce the low pressure at the core of the hurricane due to their coarser
 298 grid, leading to an overestimation of 8 mbar of the storm depression. Both
 299 H*Wind and ERA-5 agree well with observed wind speeds although both
 300 data sets tend to slightly overestimate the width and intensity of the wind
 301 peak. However, H*wind profiles better reproduce the timing of the observed
 302 peak, as ERA-5 winds tend to anticipate it. H*wind also exhibits a slightly
 303 narrower peak in wind speed, which better agrees with observations.

304 Hydrodynamic outputs of the coupled wave-current model agree well with
305 tide gauge (Fig. 6) and ADCP measurements (Fig. 7). Despite a slight
306 overestimation of the amplitude of sea surface elevation (Table 1) in fair
307 weather conditions, the timing and amplitude of the storm surges are well
308 reproduced by the coupled model. The largest model error during the surge
309 is an overestimation of 18 cm of the elevation peak at Virginia Key. The fit is
310 especially good at Naples, where both the large positive and negative surges
311 are captured by the coupled model with an error of less than 5 cm. modeled
312 2D currents were validated against depth-averaged ADCP measurements
313 at mooring stations C10, C12 and C13 (Fig. 7). As in Liu et al. (2020),
314 we performed the vector correlation analysis of Kundu (1976) to compare
315 modeled and observed current velocity vectors. Correlation coefficients (ρ)
316 between simulated and observed depth-averaged currents are 0.84, 0.74 and
317 0.73 at stations C10, C12 and C13, respectively. The average veering angles
318 are below 12°, as in (Liu et al., 2020). Furthermore, the positive bias in Table
319 1 indicates that our model tends to underestimate the southward component
320 of the currents at the different stations. As expected from a depth-averaged
321 model, the best fit with observations is obtained at the shallowest mooring
322 C10, located on the 25 m isobath, with an average veering angle of 6° and
323 smaller error statistics (Table 1).

324 The simulated significant wave height agrees well with observations on
325 the WFS, where errors on the peak value do not exceed 5% (Fig. 8). On
326 Florida's eastern shelf, errors are slightly larger and reach 20%. Although the
327 model outputs agree well with observations, a lag in significant wave height is
328 observed for all 4 buoys. Moreover, the peak in significant wave height tends
329 to be underestimated at buoys 41113 and 41114, located on the eastern shelf
330 of Florida. The same tendency is observed with the modeled wave period,
331 with mean errors inferior to 1 second on the WFS and reaching more than
332 2 seconds on Florida's eastern shelf (Table 1), as the coupled model fails
333 to reproduce the observed peak in wave period between the 7th and 8th of

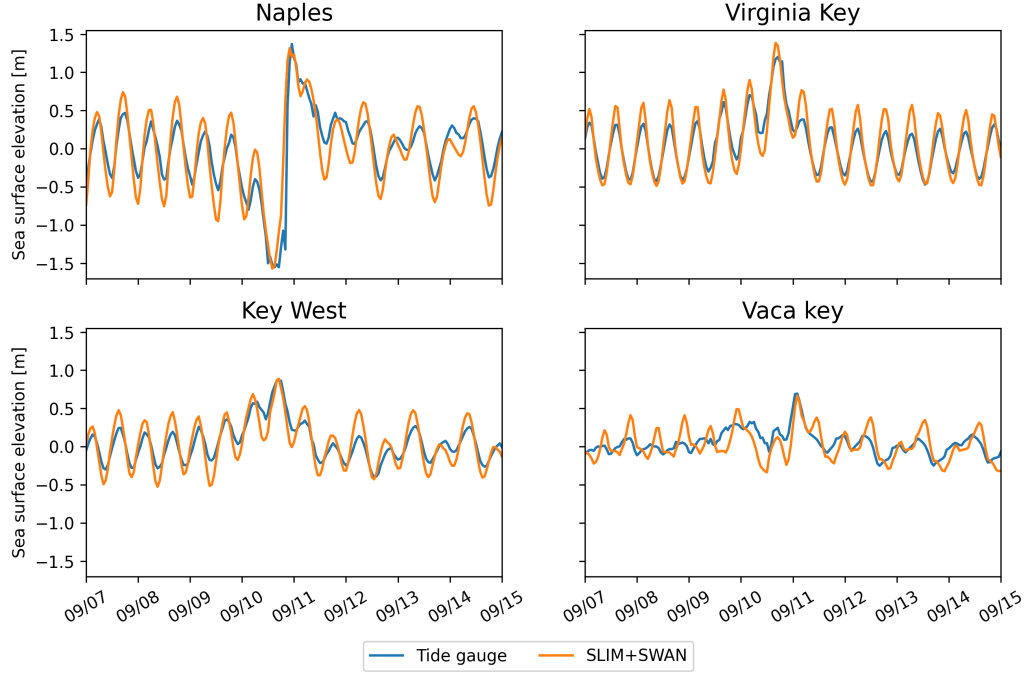


Fig. 6: Comparison of modeled sea surface elevation at the 4 tide gauges shown in Fig. 1B. The timing and amplitudes of the storm surges are well reproduced by the model

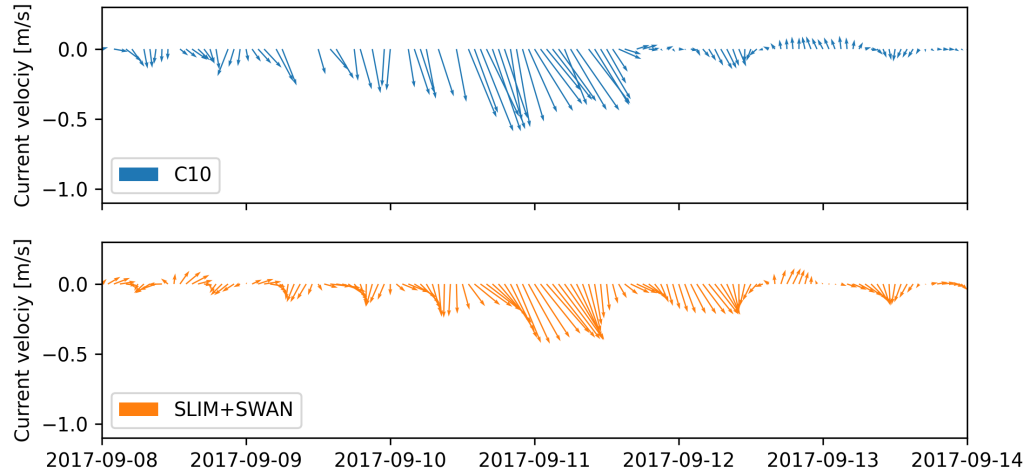


Fig. 7: Comparison of modeled current velocity with observed velocity at mooring C10 (see Fig. 1B for its location). modeled current velocities agree well with observations, with a correlation coefficient of 0.83 and an average veering angle of 6°.

334 September on this side of Florida. Finally, modeled wave direction agrees well
335 with observation (Fig. 8), although our model tends to overestimate wave
336 propagation in the northward direction at stations 41114 and 41113 on the
337 passage of the hurricane.

338 *3.2. Impact of waves on currents and transport*

339 We evaluated the impact of wave-current interactions on modeled currents
340 during the passage of Irma in the Lower Keys, between Sept. 7 and 13, 2017.
341 First, we computed the maximum difference between currents modeled by
342 SLIM and SLIM+SWAN during this period (Fig. 9A). The largest differences
343 in current speed were observed over the reefs, on the shelf break and around
344 islands. They can locally reach 1 m/s, with the coupled SLIM+SWAN model
345 yielding the largest amplitudes. The regions where the differences are the
346 largest experience the strongest radiation-stress gradient τ_{wave} (Fig. 9B)
347 induced by wave energy dissipation on the shelf-break and rough seabed
348 induce variations of the wave radiation stress (Longuet-Higgins and Stewart,
349 1964). This highlights the important protective role of the barrier formed
350 by the offshore reefs, that require a fine spatial resolution to be accurately
351 captured. Wave-induced differences in current speed were amplified by the
352 action of the wind stress τ_{wind} (Fig. 9C). Wind speeds were larger in the front
353 right quadrant of the hurricane (Zedler et al., 2009), yielding larger differences
354 on the right-hand side of the storm trajectory. This is especially clear in the
355 area between the Florida Keys and the Everglades, where relatively small
356 values of τ_{wave} nonetheless produce current speed differences of up to 0.5 m/s
357 because of the wind stress.

358 Waves play a significant role on the transport processes during and after the
359 passage of hurricane Irma (Fig. 10A,B). Comparing SLIM and SLIM+SWAN
360 shows that wave-current interactions alone yield differences of up to 5 km
361 between the modeled trajectories on the passage of the hurricane. These
362 differences exceed 10 km on the outer shelf when Stokes drift is taken into
363 account. The impact of the waves on the transport processes differs signifi-

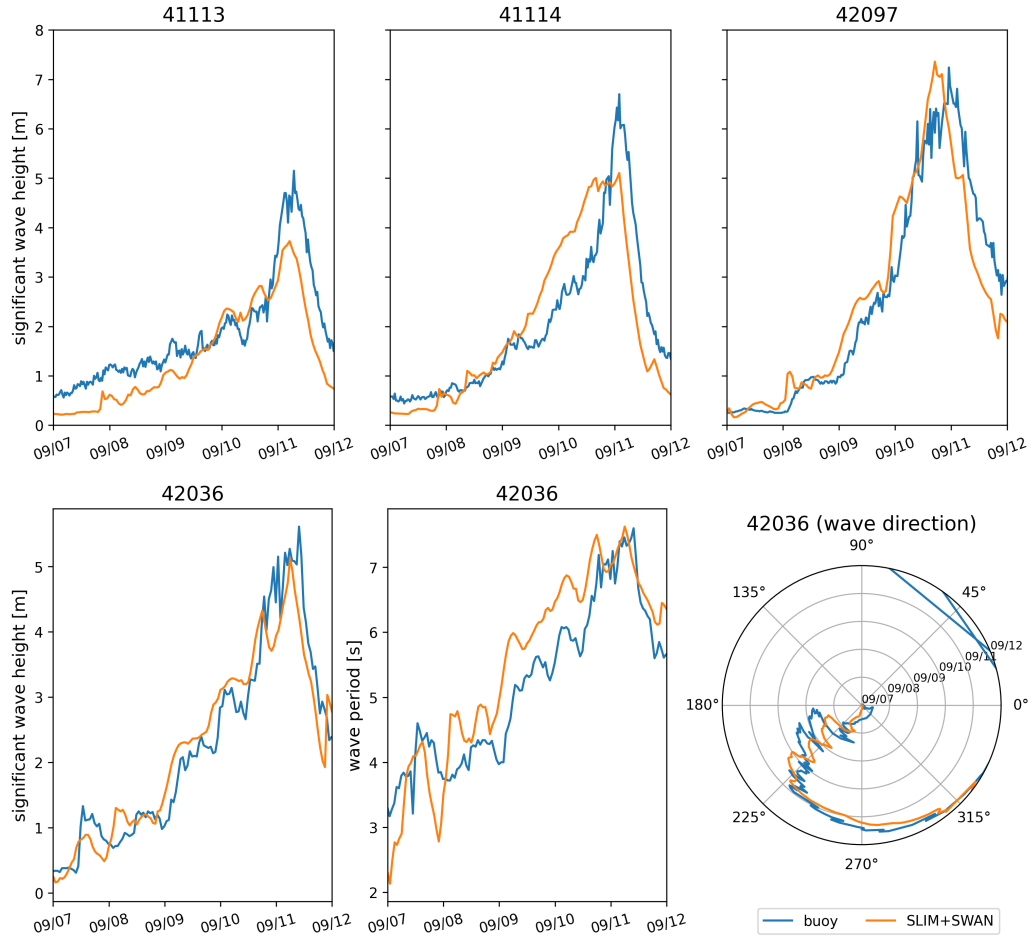


Fig. 8: Comparison of modeled wave parameters with observation at the 4 buoys location (locations shown in Fig. 1B). modeled significant wave height agrees well with field measurement.

Station	Variable	Bias	MAE	RMSE
Vaca Key	sse (m)	n/a	0.12	0.16
	U_{10} (m/s)	1.51	1.85	2.61
	p_{atm} (hPa)	-0.21	0.59	1.03
Key West	sse (m)	n/a	0.11	0.13
Virginia Key	sse (m)	n/a	0.10	0.13
Naples	sse (m)	n/a	0.18	0.23
C10	u (m/s)	-0.006	0.04	0.05
	v (m/s)	0.02	0.06	0.08
C12	u (m/s)	-0.01	0.06	0.07
	v (m/s)	0.06	0.09	0.11
C13	u (m/s)	0.004	0.06	0.08
	v (m/s)	0.04	0.06	0.08
41113	H_s (m)	-0.35	0.40	0.51
	T_m (s)	-2.18	2.47	3.13
	θ_m (degree)	7.17	19.50	26.06
41114	H_s (m)	-0.21	0.53	0.68
	T_m (s)	-1.69	2.53	3.15
	θ_m (degree)	31.25	35.28	46.18
42036	H_s (m)	-0.03	0.26	0.36
	T_m (s)	0.04	0.65	0.77
	θ_m (degree)	19.92	30.65	41.69
42097	H_s (m)	-0.15	0.40	0.57
	T_m (s)	0.02	0.62	0.74
	θ_m (degree)	3.62	28.08	45.89

Table 1: Error statistics comparing SLIM+SWAN simulated quantities with the measured sea surface elevation (sse), eastward and northward depth-average current velocities (u,v), significant wave height (H_s), zero-crossing mean wave period (T_m) and mean wave direction (θ_m). Model bias, mean absolute error (MAE), and root mean squared error (RMSE) are listed by variable (unit) and value.

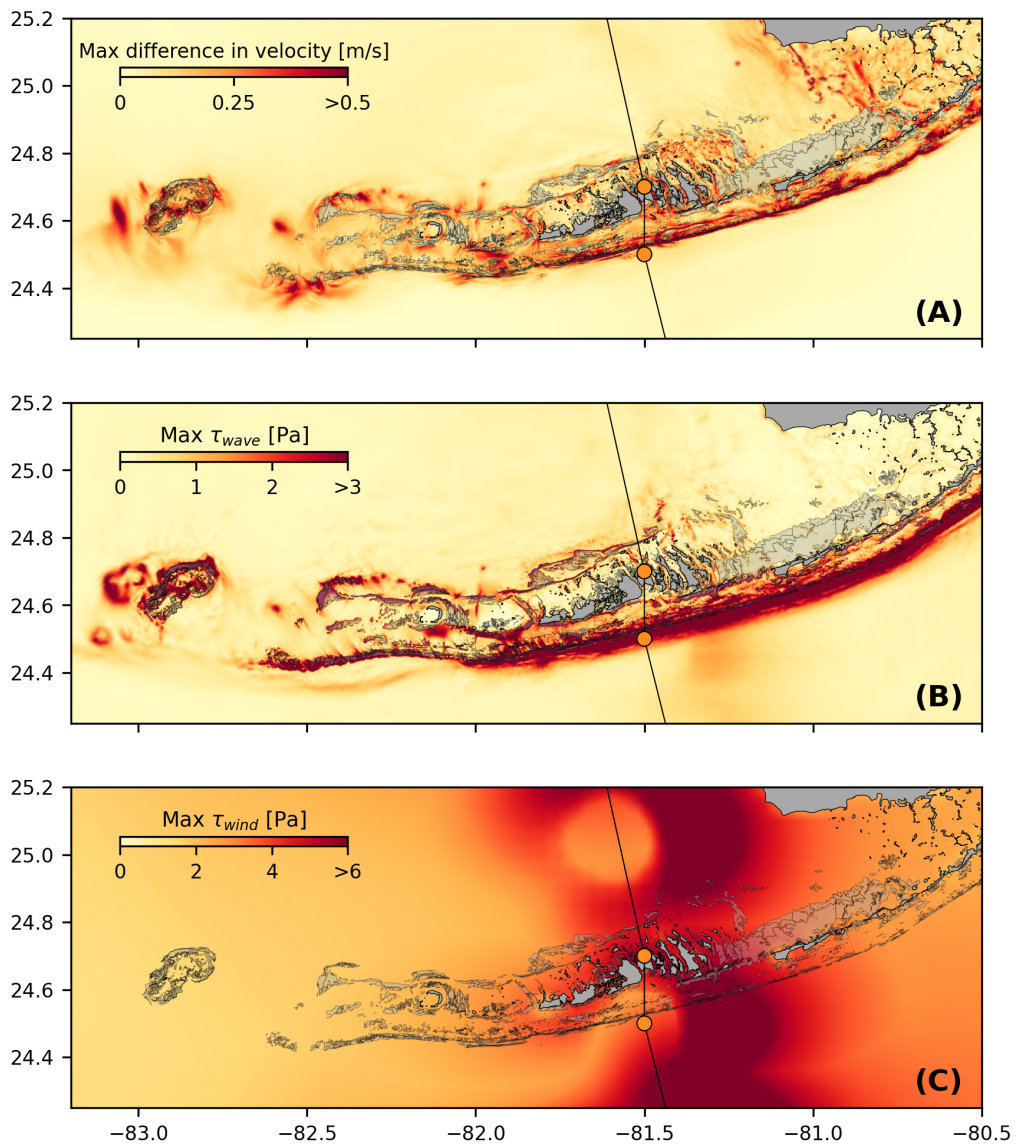


Fig. 9: (A). Maximum difference between SLIM and SLIM+SWAN currents during the passage of Irma in the Lower Florida Keys; (B) Maximum wave radiation stress gradient τ_{wave} and (C) maximum wind stress τ_{wind} (C) generated by the hurricane. Radiation stress gradient yields difference larger than 0.5 m/s (and locally reaching 1m/s) in current velocities, especially over offshore reefs.

364 cantly between the inner and outer shelves, with wave-induced differences in
365 trajectories 4 to 5 times larger on the outer shelf. Furthermore, the distance
366 between the centers of mass of the clouds of particles tends to stabilize on
367 the inner shelf after the passage of Irma, while it keeps increasing on the
368 other shelf up to two days after the passage of the hurricane when taking
369 Stokes drift into account. The distance then stabilizes for about a day before
370 it starts decreasing (see right panel of Fig. 10A,B). However, when consider-
371 ing wave-current interactions alone (SLIM vs. SLIM+SWAN), the distance
372 between the clouds of particles starts to decrease just after the passage of
373 Irma.

374 The Stokes drift appears to have a larger effect than the radiation stress
375 gradient and the wave-current interactions (Fig 10A,B). Nonetheless, compar-
376 ing the different curves for the outer shelf suggests that the radiation-stress
377 gradient induces effects similar to the impact of the Stokes drift in this
378 region during the passage of Irma. However, when comparing SLIM and
379 SLIM+SWAN both on the inner and other shelf, this impact appears to
380 be negligible during the rest of the simulation. Comparing Stokes-U and
381 Stokes-C indicates that the difference between the trajectories of particles
382 advected by the two Stokes drift do not exceed 2 km, with larger discrepancies
383 on the outer shelf (Fig. 10C,D). The distance between the two clouds of
384 particles increases abruptly on the passage of the hurricane (and two days
385 after on the outer shelf) and then stabilizes during the rest of the simulation.

386 4. Discussion

387 Validation against field measurements show that the coupled SLIM+SWAN
388 model correctly reproduces the hydrodynamics and wave dynamics during
389 hurricane Irma. Such good agreement can only be achieved using accurate
390 forcings and adequate wave parameterizations. By comparing coupled and
391 uncoupled model runs, we showed that neglecting wave radiation stress
392 gradient can induce differences of up to 1 m/s in modeled current velocities.

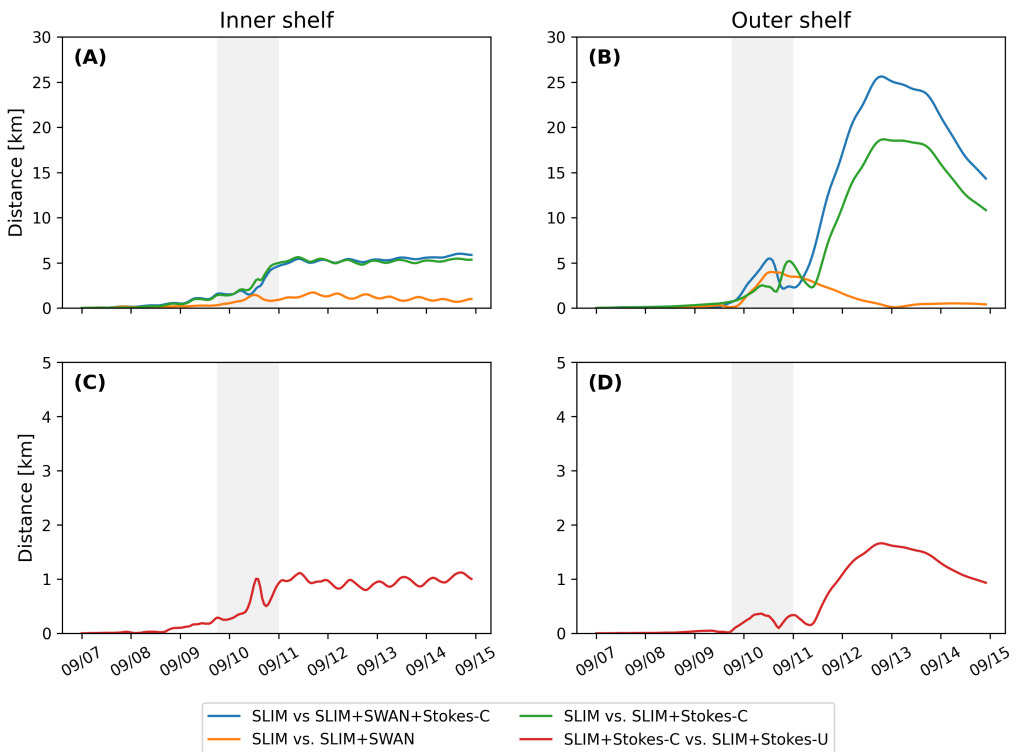


Fig. 10: Difference between the centers of mass of the particle clouds released from the regions highlighted in Fig. 4 and advected by different combinations of coupled and uncoupled velocity fields.

393 The radiation stress gradient during the hurricane was especially large over
394 the shelf break, where waves are strongly dissipated by the offshore coral reef
395 barrier. The radiation stress gradient alone can deflect drifting particles by
396 up to 5 km during the passage of the hurricane. These differences in modeled
397 trajectories were significantly larger and required more time to stabilize on
398 the outer shelf. The impact of the Stokes drift dominates the effects of
399 wave-current interactions through the radiation stress gradient, except at the
400 moment of the passage of the hurricane, when both contributions are similar.
401 Finally, neglecting wave-current interactions when computing Stokes drift
402 leads to variations of up to 2 km in modeled trajectories on the passage of
403 the hurricane.

404 Despite slightly overestimating the amplitude of the sea surface elevation in
405 fair weather conditions, the coupled wave-current model correctly reproduces
406 the timing and amplitude of the observed storm surge. All elevation peaks are
407 captured with a 4% accuracy at every stations except Virginia key, where the
408 surge was overestimated by about 15%. Such accuracy is key to predict the
409 damages caused by the hurricane, as most destroyed and severely damaged
410 buildings in the Florida keys during Hurricane Irma were caused by storm
411 surge and waves (Xian et al., 2018). Furthermore, the high resolution of
412 model in the regions captures flow accelerations between islands and reefs,
413 allowing for a precise representation of the surge risk within the Florida Keys.
414 In addition to accurately capturing positive surges, the model also reproduced
415 the observed negative surge in Naples with an error of about 1%. This result
416 is of interest from a biological point of view as negative surges, although less
417 studied, affect water exchanges between the estuaries and the coastal ocean
418 and disturb the benthic ecosystems (Liu et al., 2020). Such rapid decrease
419 in water level followed by a positive surge cause massive freshwater inflows,
420 generating a significant decrease in water salinity (Wachnicka et al., 2019).

421 Strong currents such as the Gulf Stream affect waves trough refraction
422 over gradients in current velocity, shoaling and breaking of opposing waves or

lengthening of following waves (Hegermiller et al., 2019). Under hurricane conditions, these interactions can cause numerical instabilities in the wave model if appropriate parameterizations and model resolution are not applied. Hegermiller et al. (2019), for instance, used a 5-km model grid and 48 directional bins to capture spatial gradients in wave height induced by wave-currents interactions in the Gulf Stream during Hurricane Matthew (2016). We followed these guidelines when defining the coarsest resolution of the model mesh as well as the spectral discretization of SWAN. Boundary conditions and directional spreading of the incident waves also play a significant role when modeling wave-current interactions at meso- and submesoscales (Villas Bôas et al., 2020), which motivated our choice of imposing full spectra on the boundary of the wave model instead of bulk parameters. Finally, SWAN default parameterizations for wind energy input and whitecapping caused numerical instabilities by overestimating wave growth and steepness on the boundary of the Gulf Stream on the passage of Irma. This overestimation was solved by using the parameterization of Siadatmousavi et al. (2011). The parameters used in this study were calibrated on the Northern Gulf of Mexico, which might explains that our model better reproduces wave parameters at buoys 42036 and 4207, located on the WFS. However, these calibrated parameters might underestimate wind-induced wave growth might underestimate Florida's eastern shelf. Consequently, incident wave do not receive enough energy to grow after breaking on the bank boundary, leading to the underestimation of the significant wave height at buoys 41113 and 41114. A more extensive calibration study might therefore be necessary to further improve the agreement with field measurements on both sides of Florida. Nonetheless, as this study focuses on the wave produced by Irma, which made landfall on the western coasts of Florida, the use of parameterizations calibrated for the Gulf of Mexico seems reasonable.

Radiation stress gradient significantly impacts currents during the passage of the hurricane. It can induce differences of up to 1 m/s of the current

453 velocity on the shelf break. In this region waves are strongly dissipated due to
454 action of depth-induced breaking and bottom dissipation on coral reefs. This
455 highlights the protective role of coral reefs against strong incoming waves
456 (Lowe et al., 2005), which requires a sufficiently fine spatial resolution to be
457 explicitly represented in the model. Due to the dissipation of incoming waves
458 on the reefs, wave impact during Irma is different on the inner and outer
459 shelves. It is less important on the inner shelf because of the sheltering of the
460 inner shelf due to reefs and islands as well as wave breaking on the shelf break.
461 The inner shelf hence experiences weaker waves and currents, inducing weaker
462 and more localized transport. Furthermore, the impact of winds on waves
463 is reduced in shallower areas under the action of depth-induced breaking.
464 This might explain why differences between particle trajectories stabilize
465 on the inner shelf just after the passage of Hurricane Irma. However, the
466 Florida Keys still experienced strong winds after the passage of the core of the
467 hurricane, which generated high waves in the deeper areas. This might explain
468 why the differences on between the modeled trajectories kept increasing on
469 the outer shelf under the action of strong Stokes drift up to two days after
470 the passage of the hurricane.

471 The distance between the centers of mass of the particle clouds advected
472 by coupled and uncoupled Stokes drift remains rather limited (< 2 km). This
473 suggest that taking wave-currents interactions into account when computing
474 Stokes drift, even in heavy wind conditions has a limited impact. Furthermore,
475 combining the coupled Stokes drift with the coupled and uncoupled SLIM
476 currents produced similar trajectories on the inner shelf, which seems to
477 indicate that wave impact on currents is limited in this region. This would
478 suggest that it is not necessary to take wave-current interactions into account
479 when modeling the trajectories of tracers in shallow, sheltered areas such
480 as the inner WFS during a hurricane. Uncoupled currents with uncoupled
481 Stokes drift should give a reasonably accurate approximation of the transport
482 processes. However, this does not hold for deeper and unsheltered regions,

483 as highlighted by the comparison of trajectories obtained with coupled and
484 uncoupled SLIM currents combined with coupled Stokes drift on the outer
485 shelf.

486 **5. Conclusion**

487 We developed a coupled wave-current model to study the impact of
488 waves on transport processes during Hurricane Irma. In order to accurately
489 represent the wind and pressure profiles of te hurricane, we built hybrid fields
490 by combining coarser ERA-5 data with high-resolution H*Wind data for
491 the wind speed and idealized Holland profiles for the pressure. Comparing
492 these hybrid profiles with field observations showed that they were better at
493 reproducing the observed central depression of the hurricane as well as the
494 peak in wind speed than ERA-5 data. Using these hybrid fields as forcings,
495 our coupled model accurately reproduced the storm surge at NDBC buoy
496 locations and produced currents and wave parameters in good agreement
497 with field observations, especially on the WFS. The modeled currents and
498 Stokes drift were then used to evaluate the impact of waves on the trajectory
499 of passive drifters on the passage of the hurricane through the Florida Keys.
500 Our results show that waves had a significant impact on heavy-wind transport
501 processes and caused deflections of the drifters trajectories by more than 20
502 km on the outer shelf.

503 Despite its good agreement with observations, our model could be further
504 developed by improving the representation of wind-wave interactions. In
505 particular, it does not consider the momentum loss due to the action of
506 surface waves when representing momentum flux from the atmosphere to the
507 ocean, leading to overestimations under hurricane conditions. Our model
508 could therefore be further improved by using wave-dissipative stress instead of
509 the full wind stress as the momentum flux from the atmosphere to the ocean.
510 Moreover, a more thorough calibration of the wave model parameters should
511 improve our model results on the eastern shelf of Florida. Finally, as a 2D

512 barotropic model, SLIM doesn't explicitly represent baroclinic phenomenons
513 as well as the vertical profile of the Stokes drift and radiation stress gradient
514 along the wave boundary layer. However, our study focused on relatively
515 shallow and vertically homogeneous coastal waters using a reef-scale resolution
516 throughout the whole FRT. Such fine resolution allows to explicitly represent
517 wave dissipation over coral reefs and is only achievable using 2D models due
518 to computational resources limitations.

519 Wave coupling needs to be taken into account during heavy-wind events
520 but not necessarily in milder conditions. While the radiation stress gradient
521 plays an important role and can lead to differences of up to $k \text{ km}$, the
522 Stokes drift is about 4 times more intense and should thus be considered
523 in priority. This study brings new insight on the impact of waves on the
524 transport processes nearshore during a tropical cyclone. Due to its high
525 spatial resolution, the developed coupled wave-current model can be used
526 to accurately represent the dispersal of pollutants, sediments or larvae in
527 topologically complex coastal areas in heavy-wind conditions.

528 Acknowledgments

529 Computational resources were provided by the Consortium des Équipements
530 de Calcul Intensif (CÉCI), funded by the F.R.S.-FNRS under Grant No.
531 2.5020.11. Thomas Dobbelaere is a PhD student supported by the Fund for
532 Research training in Industry and Agriculture (FRIA/FNRS).

533 References

- 534 Bever, A.J., MacWilliams, M.L., 2013. Simulating sediment transport pro-
535 cesses in San Pablo Bay using coupled hydrodynamic, wave, and sediment
536 transport models. *Marine Geology* 345, 235–253.
- 537 Bhatia, K.T., Vecchi, G.A., Knutson, T.R., Murakami, H., Kossin, J., Dixon,
538 K.W., Whitlock, C.E., 2019. Recent increases in tropical cyclone intensifi-
539 cation rates. *Nature Communications* 10, 1–9.

- 540 Booij, N., Ris, R.C., Holthuijsen, L.H., 1999. A third-generation wave
541 model for coastal regions: 1. Model description and validation. *Journal of*
542 *Geophysical Research: Oceans* 104, 7649–7666.
- 543 Breivik, Ø., Allen, A.A., Maisondieu, C., Olagnon, M., 2013. Advances in
544 search and rescue at sea. *Ocean Dynamics* 63, 83–88.
- 545 Chassignet, E.P., Hurlburt, H.E., Smedstad, O.M., Halliwell, G.R., Hogan,
546 P.J., Wallcraft, A.J., Baraille, R., Bleck, R., 2007. The HYCOM (hybrid
547 coordinate ocean model) data assimilative system. *Journal of Marine*
548 *Systems* 65, 60–83.
- 549 Chen, C., Huang, H., Beardsley, R.C., Liu, H., Xu, Q., Cowles, G., 2007.
550 A finite volume numerical approach for coastal ocean circulation studies:
551 Comparisons with finite difference models. *Journal of Geophysical Research:*
552 *Oceans* 112.
- 553 Craik, A.D., Leibovich, S., 1976. A rational model for Langmuir circulations.
554 *Journal of Fluid Mechanics* 73, 401–426.
- 555 Curcic, M., 2015. Explicit air-sea momentum exchange in coupled atmosphere-
556 wave-ocean modeling of tropical cyclones. Ph.D. thesis. University of Miami.
- 557 Curcic, M., Chen, S.S., Özgökmen, T.M., 2016. Hurricane-induced ocean
558 waves and stokes drift and their impacts on surface transport and dispersion
559 in the Gulf of Mexico. *Geophysical Research Letters* 43, 2773–2781.
- 560 Curcic, M., Haus, B.K., 2020. Revised estimates of ocean surface drag in
561 strong winds. *Geophysical Research Letters* 47, e2020GL087647.
- 562 Dietrich, J., Bunya, S., Westerink, J., Ebersole, B., Smith, J., Atkinson,
563 J., Jensen, R., Resio, D., Luettich, R., Dawson, C., et al., 2010. A high-
564 resolution coupled riverine flow, tide, wind, wind wave, and storm surge
565 model for southern Louisiana and Mississippi. Part II: Synoptic description

- 566 and analysis of Hurricanes Katrina and Rita. *Monthly Weather Review*
567 138, 378–404.
- 568 Dietrich, J., Westerink, J., Kennedy, A., Smith, J., Jensen, R., Zijlema, M.,
569 Holthuijsen, L., Dawson, C., Luettich, R., Powell, M., et al., 2011. Hurricane
570 Gustav (2008) waves and storm surge: Hindcast, synoptic analysis, and
571 validation in southern Louisiana. *Monthly Weather Review* 139, 2488–2522.
- 572 Dietrich, J.C., Tanaka, S., Westerink, J.J., Dawson, C., Luettich, R., Zijlema,
573 M., Holthuijsen, L.H., Smith, J., Westerink, L., Westerink, H., 2012. Per-
574 formance of the unstructured-mesh, SWAN+ ADCIRC model in computing
575 hurricane waves and surge. *Journal of Scientific Computing* 52, 468–497.
- 576 Dobbelaere, T., Muller, E.M., Gramer, L.J., Holstein, D.M., Hanert, E., 2020.
577 Coupled epidemic-hydrodynamic modeling to understand the spread of a
578 deadly coral disease in Florida. *Frontiers in Marine Science* 7, 1016.
- 579 Donelan, M., Haus, B., Reul, N., Plant, W., Stiassnie, M., Gruber, H., Brown,
580 O., Saltzman, E., 2004. On the limiting aerodynamic roughness of the
581 ocean in very strong winds. *Geophysical Research Letters* 31.
- 582 Drivdal, M., Broström, G., Christensen, K., 2014. Wave-induced mixing and
583 transport of buoyant particles: Application to the Statfjord A oil spill.
584 *Ocean Science* 10, 977–991.
- 585 Figueiredo, J., Baird, A.H., Connolly, S.R., 2013. Synthesizing larval com-
586 petence dynamics and reef-scale retention reveals a high potential for
587 self-recruitment in corals. *Ecology* 94, 650–659.
- 588 Fringer, O., Gerritsen, M., Street, R., 2006. An unstructured-grid, finite-
589 volume, nonhydrostatic, parallel coastal ocean simulator. *Ocean Modelling*
590 14, 139–173.
- 591 Frys, C., Saint-Amand, A., Le Hénaff, M., Figueiredo, J., Kuba, A., Walker,
592 B., Lambrechts, J., Vallaeys, V., Vincent, D., Hanert, E., 2020. Fine-scale

- 593 coral connectivity pathways in the Florida Reef Tract: Implications for
594 conservation and restoration. *Frontiers in Marine Science* 7, 312.
- 595 Geuzaine, C., Remacle, J.F., 2009. Gmsh: A 3-d finite element mesh generator
596 with built-in pre-and post-processing facilities. *International journal for
597 numerical methods in engineering* 79, 1309–1331.
- 598 Harper, B., Kepert, J., Ginger, J., 2010. Guidelines for converting between
599 various wind averaging periods in tropical cyclone conditions.
- 600 Hegermiller, C.A., Warner, J.C., Olabarrieta, M., Sherwood, C.R., 2019.
601 Wave-current interaction between Hurricane Matthew wave fields and the
602 Gulf Stream. *Journal of Physical Oceanography* 49, 2883–2900.
- 603 Hoefel, F., Elgar, S., 2003. Wave-induced sediment transport and sandbar
604 migration. *Science* 299, 1885–1887.
- 605 Holthuijsen, L.H., Powell, M.D., Pietrzak, J.D., 2012. Wind and waves in
606 extreme hurricanes. *Journal of Geophysical Research: Oceans* 117.
- 607 Janssen, P.A., 1991. Quasi-linear theory of wind-wave generation applied to
608 wave forecasting. *Journal of Physical Oceanography* 21, 1631–1642.
- 609 Johns, W.E., Schott, F., 1987. Meandering and transport variations of the
610 Florida Current. *Journal of Physical Oceanography* 17, 1128–1147.
- 611 Knaff, J.A., Sampson, C.R., Musgrave, K.D., 2018. Statistical tropical cyclone
612 wind radii prediction using climatology and persistence: Updates for the
613 western North Pacific. *Weather and Forecasting* 33, 1093–1098.
- 614 Knutson, T., Camargo, S.J., Chan, J.C., Emanuel, K., Ho, C.H., Kossin, J.,
615 Mohapatra, M., Satoh, M., Sugi, M., Walsh, K., et al., 2020. Tropical
616 cyclones and climate change assessment: Part ii: Projected response to
617 anthropogenic warming. *Bulletin of the American Meteorological Society*
618 101, E303–E322.

- 619 Komen, G., Hasselmann, S., Hasselmann, K., 1984. On the existence of a
620 fully developed wind-sea spectrum. *Journal of Physical Oceanography* 14,
621 1271–1285.
- 622 Kossin, J.P., Knapp, K.R., Olander, T.L., Velden, C.S., 2020. Global increase
623 in major tropical cyclone exceedance probability over the past four decades.
624 *Proceedings of the National Academy of Sciences* 117, 11975–11980.
- 625 Kourafalou, V.H., Kang, H., 2012. Florida Current meandering and evo-
626 lution of cyclonic eddies along the Florida Keys Reef Tract: Are they
627 interconnected? *Journal of Geophysical Research: Oceans* 117.
- 628 Kundu, P.K., 1976. Ekman veering observed near the ocean bottom. *Journal*
629 *of Physical Oceanography* 6, 238–242.
- 630 Lambrechts, J., Hanert, E., Deleersnijder, E., Bernard, P.E., Legat, V.,
631 Remacle, J.F., Wolanski, E., 2008. A multi-scale model of the hydrodynam-
632 ics of the whole Great Barrier Reef. *Estuarine, Coastal and Shelf Science*
633 79, 143–151.
- 634 Landsea, C.W., Franklin, J.L., 2013. Atlantic hurricane database uncertainty
635 and presentation of a new database format. *Monthly Weather Review* 141,
636 3576–3592.
- 637 Lane, E.M., Restrepo, J., McWilliams, J.C., 2007. Wave-current interaction:
638 A comparison of radiation-stress and vortex-force representations. *Journal*
639 *of physical oceanography* 37, 1122–1141.
- 640 Langmuir, I., 1938. Surface motion of water induced by wind. *Science* 87,
641 119–123.
- 642 Le, H.A., Lambrechts, J., Ortaleb, S., Gratiot, N., Deleersnijder, E., Soares-
643 Frazão, S., 2020. An implicit wetting–drying algorithm for the discontinuous
644 galerkin method: application to the tonle sap, mekong river basin. *Envi-
645 ronmental Fluid Mechanics* , 1–29.

- 646 Le Hénaff, M., Kourafalou, V.H., Paris, C.B., Helgers, J., Aman, Z.M., Hogan,
647 P.J., Srinivasan, A., 2012. Surface evolution of the Deepwater Horizon
648 oil spill patch: Combined effects of circulation and wind-induced drift.
649 Environmental Science & Technology 46, 7267–7273.
- 650 Lee, T.N., Leaman, K., Williams, E., Berger, T., Atkinson, L., 1995. Florida
651 Current meanders and gyre formation in the southern Straits of Florida.
652 Journal of Geophysical Research: Oceans 100, 8607–8620.
- 653 Lee, T.N., Mayer, D.A., 1977. Low-frequency current variability and spin-off
654 eddies along the shelf off southeast Florida. Collected Reprints 1, 344.
- 655 Lee, T.N., Smith, N., 2002. Volume transport variability through the Florida
656 Keys tidal channels. Continental Shelf Research 22, 1361–1377.
- 657 Lee, T.N., Williams, E., 1988. Wind-forced transport fluctuations of the
658 Florida Current. Journal of Physical Oceanography 18, 937–946.
- 659 Li, Z., Johns, B., 1998. A three-dimensional numerical model of surface
660 waves in the surf zone and longshore current generation over a plane beach.
661 Estuarine, Coastal and Shelf Science 47, 395–413.
- 662 Lin, N., Chavas, D., 2012. On hurricane parametric wind and applications in
663 storm surge modeling. Journal of Geophysical Research: Atmospheres 117.
- 664 Liu, Y., Weisberg, R.H., 2012. Seasonal variability on the West Florida shelf.
665 Progress in Oceanography 104, 80–98.
- 666 Liu, Y., Weisberg, R.H., Zheng, L., 2020. Impacts of hurricane Irma on the
667 circulation and transport in Florida Bay and the Charlotte Harbor estuary.
668 Estuaries and Coasts 43, 1194–1216.
- 669 Liubartseva, S., Coppini, G., Lecci, R., Clementi, E., 2018. Tracking plastics
670 in the Mediterranean: 2D Lagrangian model. Marine Pollution Bulletin
671 129, 151–162.

- 672 Longuet-Higgins, M.S., 1970. Longshore currents generated by obliquely
673 incident sea waves. *Journal of geophysical research* 75, 6778–6789.
- 674 Longuet-Higgins, M.S., Stewart, R., 1964. Radiation stresses in water waves;
675 a physical discussion, with applications, in: Deep sea research and oceano-
676 graphic abstracts, Elsevier. pp. 529–562.
- 677 Lowe, R.J., Falter, J.L., Bandet, M.D., Pawlak, G., Atkinson, M.J., Moni-
678 smith, S.G., Koseff, J.R., 2005. Spectral wave dissipation over a barrier
679 reef. *Journal of Geophysical Research: Oceans* 110.
- 680 Madsen, O.S., Poon, Y.K., Gruber, H.C., 1989. Spectral wave attenuation by
681 bottom friction: Theory, in: *Coastal Engineering 1988*, pp. 492–504.
- 682 Malmstadt, J., Scheitlin, K., Elsner, J., 2009. Florida hurricanes and damage
683 costs. *Southeastern Geographer* 49, 108–131.
- 684 McWilliams, J.C., Restrepo, J.M., Lane, E.M., 2004. An asymptotic theory
685 for the interaction of waves and currents in coastal waters. *Journal of Fluid
686 Mechanics* 511, 135.
- 687 McWilliams, J.C., Sullivan, P.P., 2000. Vertical mixing by Langmuir circula-
688 tions. *Spill Science & Technology Bulletin* 6, 225–237.
- 689 Mei, C.C., 1989. The applied dynamics of ocean surface waves. volume 1.
690 World scientific.
- 691 Moon, I.J., Ginis, I., Hara, T., Thomas, B., 2007. A physics-based parame-
692 terization of air-sea momentum flux at high wind speeds and its impact on
693 hurricane intensity predictions. *Monthly Weather Review* 135, 2869–2878.
- 694 Pinelli, J.P., Roueche, D., Kijewski-Correa, T., Plaz, F., Prevatt, D., Zisis,
695 I., Elawady, A., Haan, F., Pei, S., Gurley, K., et al., 2018. Overview of
696 damage observed in regional construction during the passage of Hurricane
697 Irma over the State of Florida, in: *Forensic Engineering 2018: Forging*

- 698 Forensic Frontiers. American Society of Civil Engineers Reston, VA, pp.
699 1028–1038.
- 700 Powell, M.D., Houston, S.H., Amat, L.R., Morisseau-Leroy, N., 1998. The
701 HRD real-time hurricane wind analysis system. Journal of Wind Engineering
702 and Industrial Aerodynamics 77, 53–64.
- 703 Powell, M.D., Vickery, P.J., Reinhold, T.A., 2003. Reduced drag coefficient
704 for high wind speeds in tropical cyclones. Nature 422, 279–283.
- 705 Röhrs, J., Christensen, K.H., Hole, L.R., Broström, G., Drivdal, M., Sundby,
706 S., 2012. Observation-based evaluation of surface wave effects on currents
707 and trajectory forecasts. Ocean Dynamics 62, 1519–1533.
- 708 Schott, F.A., Lee, T.N., Zantopp, R., 1988. Variability of structure and
709 transport of the Florida Current in the period range of days to seasonal.
710 Journal of Physical Oceanography 18, 1209–1230.
- 711 Siadatmousavi, S.M., Jose, F., Stone, G., 2011. Evaluation of two WAM
712 white capping parameterizations using parallel unstructured SWAN with
713 application to the Northern Gulf of Mexico, USA. Applied Ocean Research
714 33, 23–30.
- 715 Sikirić, M.D., Roland, A., Janečković, I., Tomazić, I., Kuzmić, M., 2013.
716 Coupling of the Regional Ocean Modeling System (ROMS) and Wind
717 Wave Model. Ocean Modelling 72, 59–73.
- 718 Smith, N.P., 1982. Response of Florida Atlantic shelf waters to hurricane
719 David. Journal of Geophysical Research: Oceans 87, 2007–2016.
- 720 Spivakovskaya, D., Heemink, A., Milstein, G., Schoenmakers, J., 2005. Sim-
721 ulation of the transport of particles in coastal waters using forward and
722 reverse time diffusion. Advances in water resources 28, 927–938.

- 723 Stokes, G.G., 1880. On the theory of oscillatory waves. Transactions of the
724 Cambridge Philosophical Society .
- 725 Tolman, H.L., et al., 2009. User manual and system documentation of
726 WAVEWATCH III TM version 3.14. Technical note, MMAB Contribution
727 276, 220.
- 728 Van Den Bremer, T., Breivik, Ø., 2018. Stokes drift. Philosophical Trans-
729 actions of the Royal Society A: Mathematical, Physical and Engineering
730 Sciences 376, 20170104.
- 731 Villas Bôas, A.B., Cornuelle, B.D., Mazloff, M.R., Gille, S.T., Arduin, F.,
732 2020. Wave-current interactions at meso-and submesoscales: Insights from
733 idealized numerical simulations. Journal of Physical Oceanography 50,
734 3483–3500.
- 735 Wachnicka, A., Browder, J., Jackson, T., Louda, W., Kelble, C., Abdelrahman,
736 O., Stabenau, E., Avila, C., 2019. Hurricane Irmas impact on water quality
737 and phytoplankton communities in Biscayne Bay (Florida, USA). Estuaries
738 and Coasts , 1–18.
- 739 Weisberg, R., Liu, Y., Mayer, D., 2009. Mean circulation on the west Florida
740 continental shelf observed with long-term moorings. Geophys. Res. Lett
741 36, L19610.
- 742 Weisberg, R.H., Zheng, L., 2006. Hurricane storm surge simulations for
743 Tampa Bay. Estuaries and Coasts 29, 899–913.
- 744 Wu, L., Chen, C., Guo, P., Shi, M., Qi, J., Ge, J., 2011. A FVCOM-
745 based unstructured grid wave, current, sediment transport model, I. Model
746 description and validation. Journal of Ocean University of China 10, 1–8.
- 747 Xian, S., Feng, K., Lin, N., Marsooli, R., Chavas, D., Chen, J., Hatzikyriakou,
748 A., 2018. Brief communication: Rapid assessment of damaged residential

- 749 buildings in the Florida Keys after Hurricane Irma. *Natural Hazards and*
750 *Earth System Sciences* 18, 2041–2045.
- 751 Zedler, S., Niiler, P., Stammer, D., Terrill, E., Morzel, J., 2009. Ocean's
752 response to Hurricane Frances and its implications for drag coefficient
753 parameterization at high wind speeds. *Journal of Geophysical Research:*
754 *Oceans* 114.
- 755 Zhang, C., Durgan, S.D., Lagomasino, D., 2019. Modeling risk of mangroves
756 to tropical cyclones: A case study of Hurricane Irma. *Estuarine, Coastal*
757 *and Shelf Science* 224, 108–116.